Proceedings of the ASME 2019 International Technical Conference and Exhibition on Packaging and Integration of Electronic and Photonic Microsystems
InterPACK2019
October 7-9, 2019, Anaheim, CA, USA

IPACK2019-6372

EVAPORATION RATE MEASUREMENT AT MULTIPLE SCALES USING TEMPERATURE-SENSITIVE FLUORESCENCE DYES

Youngjoon Suh[1], Cheng-Hui Lin[1], Hamsa Gowda[2], Yoonjin Won[1]

[1]Department of Mechanical and Aerospace Engineering, University of California, Irvine, CA, USA
[2]Department of Biomedical Engineering, University of California, Irvine, CA, USA

ABSTRACT

As modern electronics continuously exceed their performance limits, there is an urgent need to develop new cooling devices that balance the increasing power demands. To meet this need, cutting-edge cooling devices often utilize microscale structures that facilitate two-phase heat transfer. However, it has been difficult to understand how microstructures trigger enhanced evaporation performances through traditional experimental methods due to low spatial resolution. The previous methods can only provide coarse interpretations on how physical properties such as permeability, thermal conduction, and effective surface areas interact at the microscale to effectively dissipate heat. This motivates researchers to develop new methods to observe and analyze local evaporation phenomena at the microscale.

Herein, we present techniques to characterize submicron to macroscale evaporative phenomena of microscale structures using micro laser induced fluorescence (μLIF). We corroborate the use of unsealed temperature-sensitive dyes by systematically investigating their effects on temperature, concentration, and liquid thickness on the fluorescence intensity. Considering these factors, we analyze the evaporative performances of microstructures using two approaches. The first approach characterizes local or overall evaporation rates by measuring the solution drying time. The second method employs an intensity-to-temperature calibration curve to convert temperature-sensitive fluorescence signals to surface temperatures. Then, submicron-level evaporation rates are calculated by employing a species transport equation for vapor at the liquid-vapor interface. Using these methods, we reveal that capillary-assisted liquid feeding dominates evaporation phenomena on microstructured surfaces. This study will enable engineers to decompose the key thermofluidic parameters contributing to the evaporative performance of microscale structures.

NOMENCLATURE

Variables

C	vapor molar concentration, $molm^{-3}$
D	diffusion coefficient in air, m^2s^{-1}
h	average structural thickness, μm
h_{fg}	enthalpy of evaporation, Jkg^{-1}
I	fluorescence intensity, a.u.
L	length, mm
m	mass, kg
M	molecular weight, $kgmol^{-1}$
$\dot{m}"$	mass flux, $kgm^{-2}s^{-1}$
p	pressure, Pa
P	fitting coefficient, K
R	universal gas constant, $Jmol^{-1}K^{-1}$
t	time, s
T	absolute temperature, K
u	fluid velocity, ms^{-1}
v	speed, μms^{-1}

Subscripts

air	air
atm	atmospheric pressure
far	$3h$ distance from liquid-vapor interface
ld	local drying
lv	liquid-vapor interface
n	component along $\vec{n}$ direction
od	overall drying
ref	reference
sat	saturated
tot	vapor and air
v	vapor

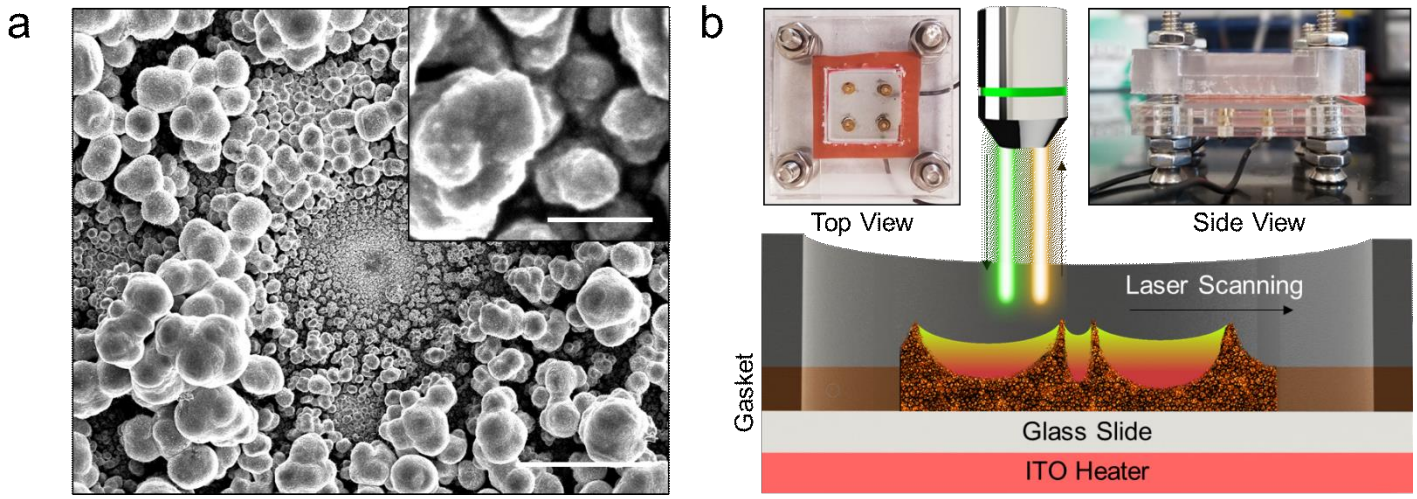

FIGURE 1: EXPERIMENTAL SETUP TO MEASURE EVAPORATIVE PERFORMANCE OF MICROSCALE STRUCTURES. (a) The porous structures used in this study show a highly interconnected network of coarse and fine copper particles as confirmed by the scanning electron microscope (SEM) image. The scalebar is 100 μm. Inset shows a magnified image of copper particles where the scalebar represents 2 μm. (b) The sample is mounted onto a glass slide where a heat flux of 0.75 Wcm^{-2} is applied by an indium-tin-oxide (ITO) heater. A fluorescence dye solution is supplied through the porous copper structure and is excited by 559 nm wavelength laser (green). The emitted light (yellow) passes through optical filters and is processed using a computer software to provide fluorescence imaging. The upper left and right insets show the top and side view of the chip, respectively.

1. INTRODUCTION

Over the past several decades, modern electronics continuously exceed their performance limits and get smaller, stimulating needs to develop high-performance cooling devices that meet the increasing power density.[1] Among various cooling apparatus, two-phase cooling devices, such as vapor chambers,[2] capillary pumped loop heat pipes,[2, 3] loop heat pipes,[2-5] and thermosyphon heat pipes,[6] have shown great potential as a remedy for thermal management issues. In general, these devices operate in an evaporation, liquid-transport, and condensation cyclic system, and utilize micro/nanoscale structures called the wick (Figure 1a).[2] The wick plays a vital role in designated parts of the cooling device by vaporizing, absorbing, and transporting the working fluid to maximize heat dissipation. The wick's role in the heat pipe system underlines the importance of understanding quantitative impacts of micro/nanostructures on evaporation phenomena. A general consensus of an optimal wick includes their properties such as efficient working-fluid delivery (i.e., permeability),[4] large surface area to volume ratios,[7] low thermal resistance,[6] and high effective thermal conductivity.[6]

Past experimental heat transfer literatures analyze the wick's heat transfer (i.e., evaporative) performances in relatively path independent approaches.[4, 8-10] In other words, these experimental methods rely on macroscale results rather than the results derived from microscale thermofluidic processes. This "low spatial resolution approach" makes it difficult to precisely predict the wick's overall evaporative performance, which involves interplaying thermophysical parameters such as permeability, thermal conductivity, and effective surface areas. Analyzing local evaporative performances is thereby important to identify how those properties correspond to the heat dissipation at the device level. Among various methods to examine evaporation rates, a proven method is to measure local surface temperature profiles and insert them into energy balance equations or diffusion mass balance equations.[11-15]

Measuring small-scale thermal profiles is challenging, and numerous temperature measurement methods have emerged to address resolution limitations. For example, infrared (IR) thermography measures two-dimensional temperature profiles based on sample thermal emission.[11, 16-19] However, IR imaging is limited to the scales above 3 – 5 μm due to the wavelength diffraction limit measured in the camera (> 3 μm).[18, 20] Another popular method is thermochromic liquid crystal thermography (TLC), which uses temperature-sensitive colors reflected by crystals to measure temperatures with up to 0.1 K thermal resolution.[12, 18, 21-23] While TLC measurements support high resolution, the samples need additional treatment such as thin and uniform coatings to increase spatial resolution,[18, 23] which makes it unsuitable for observing unpaintable objects such as porous material.[18] Direct measurement employing scanning thermal microscopy (SThM) uses nanoscale probe apexes to map thermal profiles at high-resolutions (~30 nm).[24-26] However, the contact area of the probe to the sample can vary depending on the local sample geometry, which can lead to contact-related artifacts.[27, 28] Finally, micro-thermocouple probes prove the most conventional among the measuring techniques; they are cheap and accurate, but too large to probe into submicron-level features without damaging the structure (i.e., smallest micro-thermocouple commercially available is 13-50 μm).[23]

As an emerging technique, laser induced fluorescence (LIF) gains attention as a powerful tool to characterize thermal profiles at various scales. In general, LIF utilizes temperature-and light-sensitive molecules called fluorophores. At the macroscale, LIF has been conventionally used to analyze bulk thermofluidic physics typically over the mm scale.[29-31] On the other hand, micro laser induced fluorescence (μLIF) employs fluorescent microscopes to improve spatial and thermal resolutions up to 0.1 – 0.3 μm and 0.01 K, respectively. [20, 32-38] The methods generally employ fluorescence, where temperature-sensitive fluorophores absorb photons of a specific wavelength (i.e., excitation) and emit photons of a longer wavelength (i.e., emission) (Figure 1b). The emitted fluorescence signals are selectively transmitted through an optical filter to produce fluorescence intensity-based imaging, which is then converted into temperature-based pictures. A great advantage of using μLIF is to observe temporal micro/nanoscale pixel-based fluorescent intensity profiles of the liquid-vapor interface. In other words, even some of the smallest liquid-vapor surface features are easily detected by observing fluorescence signals and can be used to assess local drying phenomena in complex structures. Although μLIF techniques have shown potential to function as thermometers in closed systems,[20, 33, 36] there are several inherent problems that could affect the measurement accuracy in an open system (where solvent is evaporating) such as photobleaching and thin-film evaporation. Photobleaching terminally alters the fluorophores and make them unable to fluoresce, but can be minimized by selecting certain dyes and with careful control over the laser beam intensity.[20, 39] On the other hand, the thin-film solvent evaporation effects on fluorescence behavior is not as simple to address because the liquid film thickness and dye concentration simultaneously change upon evaporation. Past studies report that fluorescence intensity increases with larger liquid thickness or with higher dye concentration.[40, 41] However, the integrated effect of such two factors on fluorescence intensity remains unexplored.

Herein, we systematically present methods to characterize microscale evaporative phenomena in an open system by using μLIF techniques. For this, we investigate temperature, liquid thickness, and concentration effects on fluorescence intensity. Then, we analyze evaporative phenomena at the large (~1 cm) and local (0.3 – 35 μm) scales by employing μLIF techniques. Finally, we use vapor transport equations to calculate submicron level evaporation rates based on measured surface temperatures. Our results help decompose key physical parameters such as microscopic liquid flow paths that influence the wick's evaporative performance. Therefore, the insights of this study can promise technical advances towards applications requiring high-fidelity microscale thermophysical characterization.

2. EXPERIMENTAL METHOD

2.1 Rhodamine B Solution

We use laser grade rhodamine B (Acros Organics) to make a temperature-sensitive fluorescent working fluid. Prior to rhodamine B addition, a 0.1 M sodium carbonate-bicarbonate buffer at pH 9.4 is prepared to ensure proper dye color density. The buffer is made by adding 30 ml of 0.1 M sodium carbonate to 70 ml of 0.1 M sodium bicarbonate. The buffer is then diluted from 0.1 M to 0.2 mM, and rhodamine B is added to make a 2 mM solution. The rhodamine B solutions are filtered with a syringe filter (0.2 μm pore size) before the use.

2.2 Evaporation Chip Fabrication

In order to test the evaporation phenomena at elevated temperatures, we prepare an evaporation chip. The evaporation chip consists of top and bottom acrylic platforms, a removable glass slide, a rubber gasket, spring-loaded pogo pins, and a transparent indium-tin-oxide (ITO) heater. The top and bottom platforms are fabricated using a computer numerical control (CNC) router to provide rigid support for all components. The gasket is inserted between the glass slide and the top chip to prevent leakage by applying distributed pressure through bolts and nuts. A constant voltage is provided through a power supply to produce a constant heat flux of 0.75 Wcm^{-2} from the ITO heater to the glass slide.

2.3 Fabrication Process of Microscale Structures

The wicks are fabricated using a simple template-assisted electrodeposition method. A 1 mm thick brass plate is cut into 1 cm × 3 cm sample pieces through machining processes. A copper sample used as the anode is prepared with identical dimensions. The brass and copper samples are immersed in hydrochloric acid for 15 minutes prior to electrodeposition. The electrodeposition process is performed in a stationary 0.4 M $CuSO_4$ + 1.8 M H_2SO_4 solution. A constant current density of 2 Acm^{-2} is applied for 3 minutes with a power supply.

2.4 Image Acquisition

To obtain real-time, fluorescence-based liquid-vapor interface images, we use both inverted and upright confocal fluorescence microscopes. The inverted microscope views objects from bottom to top and can greatly increase imaging precision by eliminating the need to continuously focus on dynamic liquid-vapor interfaces. Accordingly, we use an inverted microscope (LSM 700, ZEISS) with a 10 mm long working distance objective to characterize the liquid thickness and concentration effects on fluorescence intensity. An appropriate filter set (559 nm excitation band pass and 570-800 nm emission band pass) with a broadband halogen illumination is used.

On the other hand, the upright microscope enables surface imaging of opaque samples from top to bottom when the excitation light cannot penetrate through the sample. Hence, an upright microscope (BX61, Olympus) is used to characterize evaporative performances of opaque microscale structures. A minimal laser beam intensity of 0.3% (to reduce photobleaching) excites the fluid at wavelengths of 559 nm to fluoresce while a fluorimeter records the fluorescence spectra. The high voltage (HV) and gain are set manually and are kept constant throughout a given set of experiments. Digital images are obtained and post-

processed with ZEN (ZEISS) and FluoView FV1000 (Olympus) software. Image colors are added using built-in channel options.

3. MATHEMATICAL MODEL

In section 4.2.3, we calculate local evaporation rates based on surface temperatures by employing a species transport equation for vapor at the liquid-vapor interface.[14, 15] By assuming that the equilibrium vapor pressure at the interface $p_{v\_equ}(T_{lv})$ is equivalent to the saturation pressure, the Clausius-Clapeyron equation can provide an expression for the saturation pressure $p_{sat}(T_{lv})$:

$$p_{v\_equ}(T_{lv}) \approx p_{sat}(T_{lv}) = p_{sat\_ref}(T_{lv}) \exp\left(\frac{Mh_{fg}}{R}\left(\frac{1}{T_{sat\_ref}} - \frac{1}{T_{lv}}\right)\right) \quad (1)$$

where $p_{sat\_ref}(T_{lv})$ is the reference saturation pressure of 1 atm, M is the vapor molecular weight, h_{fg} is the latent heat, T_{sat_ref} is the reference saturation temperature at 1 atm, R is the universal gas constant, and T_{lv} is the liquid-vapor temperature. On the other hand, the mass flux (i.e., evaporative mass flux $\dot{m}''$) at the liquid-vapor interface is provided through a general species transport equation:

$$\dot{m}_v'' = M(-D\vec{n} \cdot \nabla C_v + u_n C_v) \quad (2)$$

where D is the diffusion coefficient, u is the fluid velocity, and C is the molar concentration. A similar equation can be written for air. Since there is no mass transport of air ($\dot{m}_{air}'' = 0$) through the interface, the species transport equation for air becomes:

$$u_n|_{lv} = \frac{D}{C_{air}}(\vec{n} \cdot \nabla C_{air})|_{lv} \quad (3)$$

$$= -\frac{D}{C_{tot} - C_v}(\vec{n} \cdot \nabla C_v)|_{lv} \quad (4)$$

By substituting this to Eq. 2:

$$\dot{m}_v'' = -\frac{MD}{1 - C_v/C_{tot}}(\vec{n} \cdot \nabla C_v)|_{lv} \quad (5)$$

According to the ideal-gas law:

$$C_{tot}|_{lv} = \frac{p_{atm}}{RT_{lv}} \quad (6)$$

$$C_v|_{lv} = \frac{p_{sat}(T_{lv})}{RT_{lv}} \quad (7)$$

Finally, ∇C_v is defined as:

$$\nabla C_v = \frac{C_v|_{lv} - C_v|_{far}}{3h} \quad (8)$$

where $C_v|_{lv}$ is the molar concentration at the interface and $C_v|_{far}$ is the molar concentration at a distance $3h$, where h is the average structural thickness.

4. RESULTS AND DISCUSSION

4.1 Rhodamine B Characterization

In this section, we corroborate the feasibility of using unsealed rhodamine B to characterize evaporative phenomena by systematically investigating the effects of temperature, liquid thickness, and concentration on fluorescence intensity.

4.1.1 Temperature Effect on Fluorescence Intensity. We investigate the dye's temperature-sensitivity by recording its fluorescence intensity and temperature profiles by using a heated microchip. We minimize temperature variations within the microchip by using small dimensions (1 cm X 1 cm X 0.1 cm). Prior to imaging, the microchip is heated to ~75°C using a hotplate. Fluorescence images are captured every second as the microchip cools down while the solution temperature is recorded every 10 seconds with a pre-installed thermocouple. The fluorescence intensity increases as the solution temperature decreases as shown in Figure 2a. The fluorescence intensities are then normalized by the fluorescence intensity measured at room temperature (25°C), resulting in a calibration curve (Figure 2b), which is a fourth-order polynomial fit to the data of the form:

$$T = P_o + P_1 I + P_2 I^2 + P_3 I^3 + P_4 I^4 \quad (9)$$

where T is the temperature, I is the normalized fluorescence intensity, and $P_o - P_4$ are fitting constants: P_o = (128.7 ± 2.6)°C, P_1 = (-359.5 ± 20.3)°C, P_2 = (589.9 ± 54.8)°C, P_3 = (-499.4 ± 61.5)°C, and P_4 = (165 ± 24.5)°C. The fitted line is relatively consistent even at different dye concentrations (Figure 2a-b) and matches very well with the past report of Ross et al.[36]

4.1.2 Liquid Thickness Effect on Fluorescence Intensity. To understand the liquid thickness effect on fluorescence intensity, we analyze a liquid meniscus trapped between two glass slides separated by 1 mm. The focal plane is fixed by focusing on a mark created at the bottom of the glass slide, as shown in Figure 2c. The meniscus is generated by pipetting 200 µl of rhodamine B solution between the glass slides. We discover an almost linear increase in fluorescence intensity until the liquid thickness reaches ~500 µm (Figure 2d). This is because the light passes through more solution at constant dye concentrations, thereby exciting more fluorophores. However, the fluorescence intensity reaches a plateau when the distance that light can penetrate through the solution is equal to the maximum distance that fluorescence can be sensed (Figure 2d). This relationship between liquid thickness and fluorescence intensity holds for different temperatures (Figure 2d). All these results infer that varying liquid thickness has substantial influence on fluorescence intensity when the liquid thickness is < 500 µm but is less sensitive when liquid thicknesses is > 500 µm. Therefore, we minimize the effect of liquid thickness by

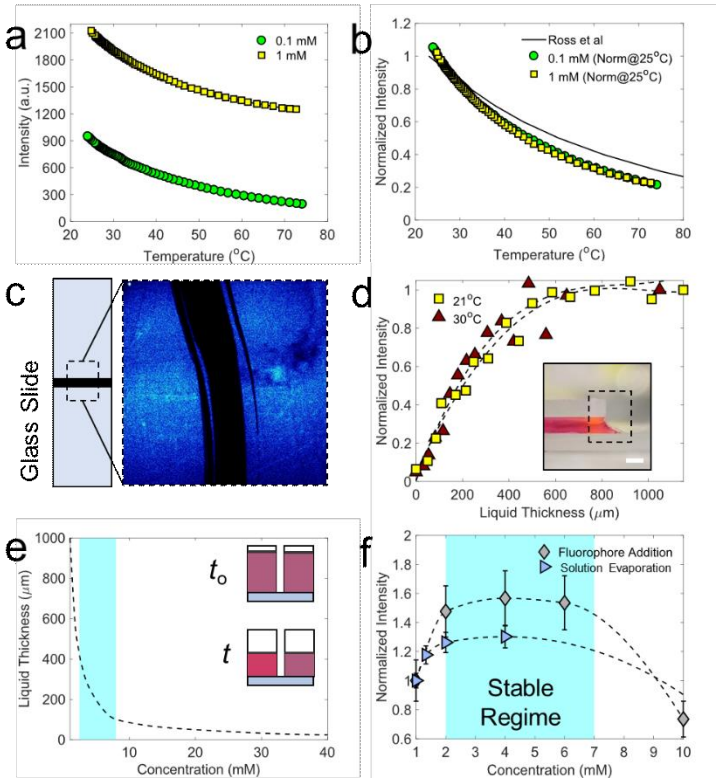

FIGURE 2: CHARACTERIZATION OF RHODAMINE B SOLUTION. (a) The plot shows that the fluorescence intensity of rhodamine B decreases as temperature increases. The decreasing trend is relatively independent of concentration. It should be noted that the gain of the 1 mM concentration case is set to a lower value than the 0.1 mM case due to excessive fluorescence signals. (b) The calibration curve is created by normalizing the raw intensity values at room temperature, 25°C. The calibration curve shows excellent consistency between different concentrations and a good match with a previous research by Ross et al. (c) The focal length is fixed by maintaining a constant focus on the bottom slide. The focal length is initially determined by focusing on a marker as shown. (d) The fluorescence intensity exhibits an almost linear increasing trend with liquid thickness up to ~ 500 μm. The measured fluorescence intensity values are normalized with intensity peak values for each experiment. Inset shows how a meniscus is formed between two glass slides. The scale bar is 1 mm. (e) A concentration estimation curve of an evaporating solution is plotted where the liquid thickness represents the amount of solution left. Insets show liquid thicknesses at different time frames. (f) The concentration effect on fluorescence intensity is plotted, showing the existence of a stable regime that is relatively independent of concentration between 2 – 7 mM.

maintaining a constant liquid thickness through a reservoir in later sections.

4.1.3 Concentration Effect on Fluorescence Intensity. We quantify how dye concentration impacts fluorescence intensity in an open system environment. To do this, we compare two cases: In one case, we increase the dye concentration by evaporating the dye solution. In the second case, the dye concentration is kept constant while the liquid thickness is adjusted to match the former case. In detail, two 1 cm-diameter wells are filled with 1 mM rhodamine B solution, as shown in the inset of Figure 2e. The solution of one well is exposed to air at room temperature to promote evaporation, whereas the other is sealed to prevent it. The liquid thickness and fluorescence intensity are measured for both wells in sequential timesteps where the second well's solution is pulled out manually every timestep to match the first well's liquid thickness. We discover that the first well's fluorescence intensity increases as the solution evaporates while the second well's fluorescence signal remains constant above liquid thickness of 1 mm which agrees with the previous section. We proceed to plot the estimated evaporation-induced concentration variations with respect to liquid thickness from a known initial fluorophore mass (Figure 2e). The fluorescence intensity increases 30% as the concentration increases from 1 mM to 2 mM but reaches a relatively stable regime at concentrations 2 – 7 mM (Figure 2f). This trend is further validated through a separate case where concentration is increased by adding fluorophores at a fixed volume (Figure 2f). The 15% – 20% error between the two approaches may be attributed to fluorophores escaping the liquid through evaporation or by adhering to the surrounding walls. The drastic fluorescence intensity drop after the stable regime is caused by the self-quenching of fluorophores and has been reported elsewhere.[40] In other words, our results show that ~90% of the experimental process occurs at concentrations between 1 – 10 mM. In this study, we use 2 mM dye concentration as an effort to reduce concentration effects.

4.2 Characterization of the Wick's Evaporative Performance

To analyze the wick's heat transfer performance, we characterize evaporative phenomena of the liquid at different scales using fluorescence signal tracking and fluorescence thermometry methods. For the following experiments, the sample heats up at a constant heat flux of 0.75 Wcm^{-2} with an ITO heater installed at the base of the chip. As the solution evaporates, the liquid thickness reduction decreases the fluorescence intensity. However, fluorophore residues emit a faint signal and prevents the fluorescence intensity from approaching zero even when the solution is depleted. Therefore, the signals emitted from residue fluorophores are defined as the background intensity. Finally, we define the background-subtracted fluorescence intensity values as the relative fluorescence intensity.

4.2.1 Overall Evaporation Rate. We measure the overall evaporation rate by tracking the surface fluorescence signals (i.e., surface-tracking) of an evaporating 10 μl rhodamine B solution droplet pipetted into the wick as shown in Figure 3a and b. As the solution surface approaches depletion, the fluorescence intensity rapidly decreases due to liquid thickness effects (Figure 2d). We define the time that the relative intensity decays to 1% of its original value as the overall dry-out time t_{od}. Figure 3c exhibits real-time fluorescence imaging of the surface-tracking method and shows incremental wick features (i.e., green colored

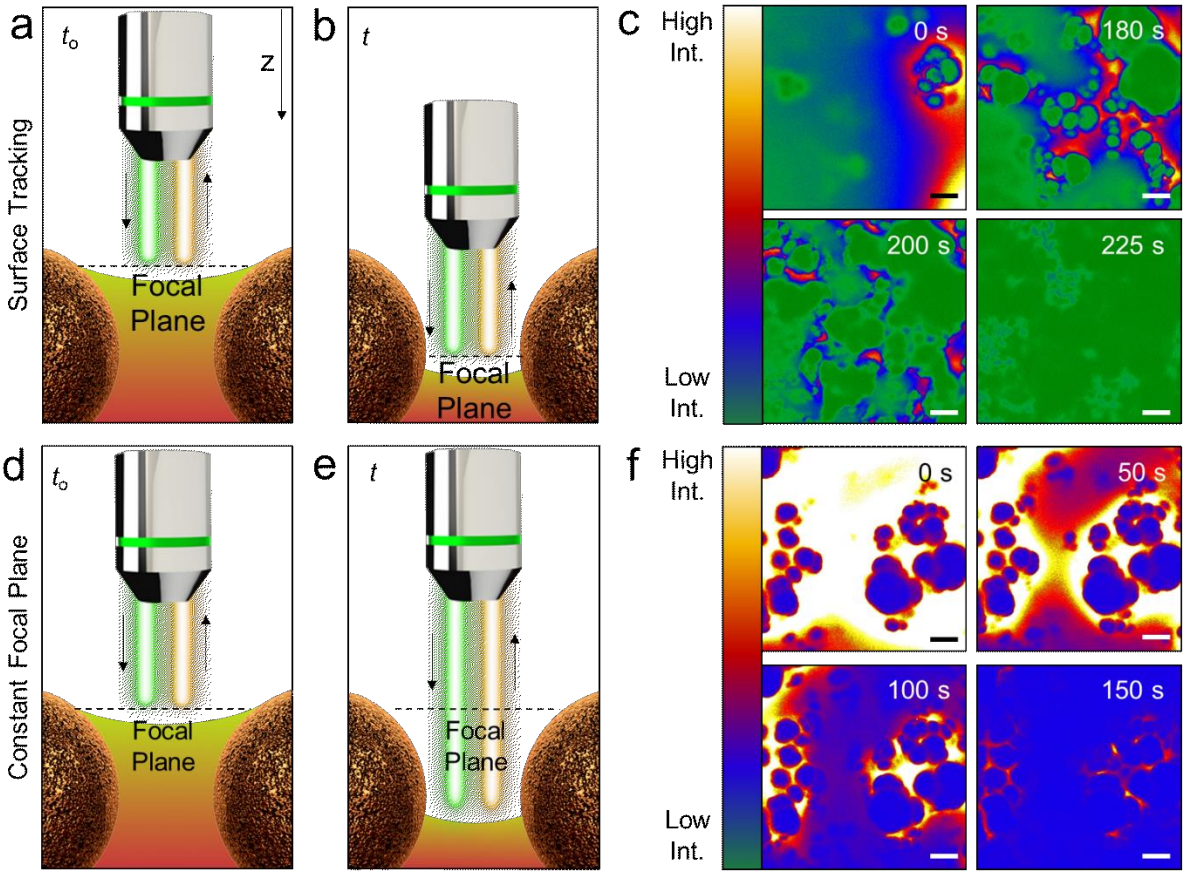

FIGURE 3: OVERALL AND LOCAL EVAPORATION RATE CHARACTERIZATION. (a-c) In the surface-tracking method, the liquid-vapor interface moves along the *z*-axis as the rhodamine B solution evaporates. The fluorescence signal emitted from the liquid-vapor interface is tracked by changing the focus plane (surface-tracking method). (a and b) The figures illustrate the surface-tracking method where (a) is the initial state and (b) is an arbitrary state during the process. (c) Real-time fluorescence images show the fluorescence intensity decay as the rhodamine B droplet evaporates. The scale bar represents 20 μm. (d-f) Unlike the surface-tracking method, the local evaporation rate is characterized by maintaining focus on a consistent plane (d) before and (e) during the evaporation process. (f) Temporal fluorescence images show that the fluorescence intensity decays as the solvent evaporates. The scale bar is 20 μm.

circles) along the z-axis. The presence of more solid materials at the base of the substrate cause the perceptional growth of the wick features shown in increasing timesteps. It should be noted that the excitation light's inability to penetrate through the solid materials causes the wick structures to have low fluorescence intensity profiles. Finally, the overall evaporation rate, defined as the ratio of the evaporated mass to t_{od}, is calculated as 4.44e-5 kgs^{-1}.

4.2.2 Local Dry-out. As an effort to untangle the strongly linked microscale phenomena that constitutes the wick's overall evaporative performance, we observe microscale (2 – 35 μm) local dry-outs. The following experiments follow the same procedures mentioned above but maintain a consistent focal plane (i.e., static focal plane), as shown in Figure 3d and e. Figure 4f shows time-dependent images of decaying fluorescence signals on the focus. In this set of experiments, the fluorescence intensity decreases as the retreating surface (or increasing focal length) impedes signal transmission. We record temporal fluorescence intensity profiles of different liquid-vapor surface areas (i.e., menisci) characterized by taking the average width (i.e., characteristic length) between solid structures, as shown in Figure 4a. Analogous to t_{od}, the elapsed time for the relative fluorescence intensity to decrease to 1% of its original value indicates the local dry-out time t_{ld}. In addition, the local drying speed u_{ld}, which is calculated by dividing the average structural height by t_{ld} characterizes microscale dry-out. u_{ld} increases almost linearly with longer characteristic lengths, which implies that liquid sections with larger liquid-vapor interface areas dries faster than sections with smaller ones.

4.2.3 Local Evaporation Rate. We finally investigate submicron level (~0.3 μm) local evaporation rates by utilizing the dye's temperature-sensitive properties. This procedure consists of three steps: (1) measuring surface fluorescence

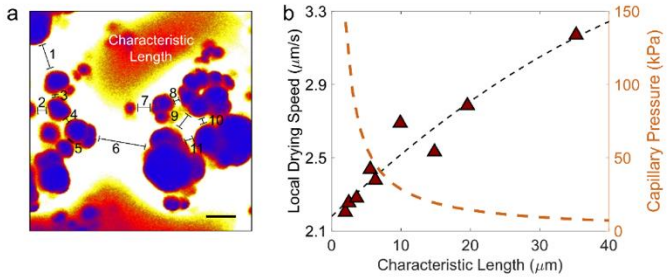

FIGURE 4: MICROSCALE DRY-OUT. (a) The image shows examples of characteristic lengths of the liquid-vapor surface area between solid particles (blue color). The blue color indicates that the solid particles have low fluorescence intensity profiles which can be attributed to the inability of the excitation light to penetrate through solid materials. The scale bar is 20 μm. (b) The local drying speed shows an almost linear increasing trend with longer characteristic length, indicating that the solution dry-out occurs faster for longer characteristic lengths. The capillary pressure estimation plot based on the feature sizes show that domains with shorter characteristic lengths provide larger capillary forces.

intensity of a heated solution in a steady state, (2) converting the measured fluorescence intensity to surface temperature, and (3) calculating local evaporation rates based on the obtained surface temperature profiles.

In the following experiment, a 300 μl reservoir maintains a constant liquid thickness within the porous structure upon evaporation (Figure 5a). The initial (i.e., cold field) (Figure 5b) system assumedly reaches a steady state (Figure 5c) when the fluorescence intensity contours remains noticeably unchanged for at least 400 seconds. Furthermore, the borderline located between the liquid and solid contours (approximately 0.3 – 1 μm from the solid contour) represents the micro regime. Next, we normalize the fluorescence intensity values of the bulk liquid surface and the micro regime by the cold field bulk liquid surface intensity.

Fitting the normalized fluorescence intensity values of the bulk liquid surface and the micro regime into the calibration curve, Eq. 9 produce local surface temperature information of both domains. The converted average surface temperatures of the bulk liquid surface and the micro regime are 34.9°C and 40.9°C, respectively.

As the final step, we calculate the local evaporative mass flux by applying the converted surface temperature values into Eq. 5. The obtained evaporation rates of the bulk liquid and micro regime are 7.4e-3 and 0.011 $kgm^{-2}s^{-1}$, respectively.

4.3 Microscopic Liquid Pathways

Our results not only characterize overall and local evaporative phenomena but also explains microscopic liquid flow paths occurring within microscale structures. In this investigation, we discover highly evaporative areas (i.e., micro regimes) near (~0.3 – 1 μm) the solid-vapor-liquid interfaces. When compared to the bulk regime, the micro regime exhibits a ~50% increase in evaporative mass flux (Figure 6a). The high evaporation associated with the micro regime (also identified as

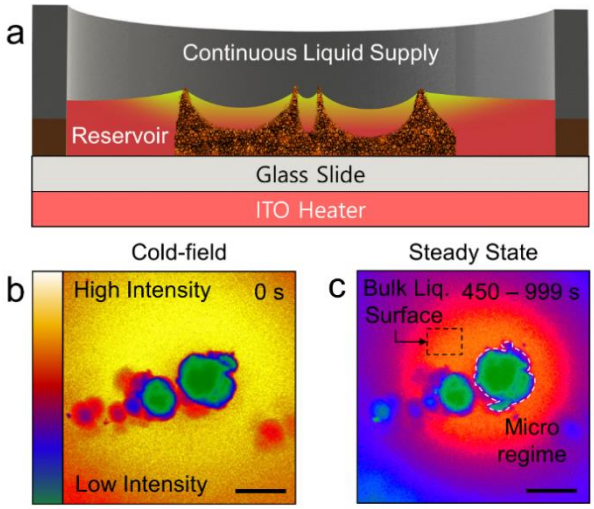

FIGURE 5: LOCAL EVAPORATION RATE MEASUREMENT. (a) A reservoir continuously supplies liquid to the wick to maintain constant liquid levels during the experiment. Average fluorescence intensities are measured for both the (b) cold-field and (c) steady state. The micro regime is visually identified by sharp fluorescence intensity-based color contrasts at the peripheral of the solid structure. The bulk liquid surface is approximately 10 μm apart from the solid particle where fluorescence intensity has a relatively uniform profile. The scale bar represents 20 μm.

the thin-film region in some papers) studies agrees with previous reports where the micro regime is found to contribute up to 80% of the overall heat transfer occurring from the entire meniscus.[42-44] A recent CFD study reports higher evaporation rates at liquid-vapor interfaces with smaller characteristic lengths.[44] In other words, liquid domains with smaller menisci have high evaporation rates because a larger portion of the menisci is influenced by the micro regime. However, we report shorter local drying speed for smaller characteristic lengths (Figure 4b) which may seem counterintuitive to the prior statement. We attribute this to the capillary pressure associated with different feature sizes, (Figure 4b). The capillary pressure estimation plot provided in Figure 4b indicates significant increases in capillary pressure as the characteristic length decreases, leading to enhanced capillary filling between smaller feature sizes. This potentially explains why smaller feature sizes can exhibit longer local drying speeds despite having higher evaporation rates as illustrated in Figure 6b. Since recent characterization of nanoscale meniscus pull-off forces (i.e., meniscus strength) suggests that the meniscus size can be tuned by varying heating temperatures,[25, 26] we conclude that liquids with small characteristic lengths (i.e., small meniscus) can maintain high evaporative performances by optimizing the balance between local evaporation rate (i.e., heating temperature) and capillary filling.

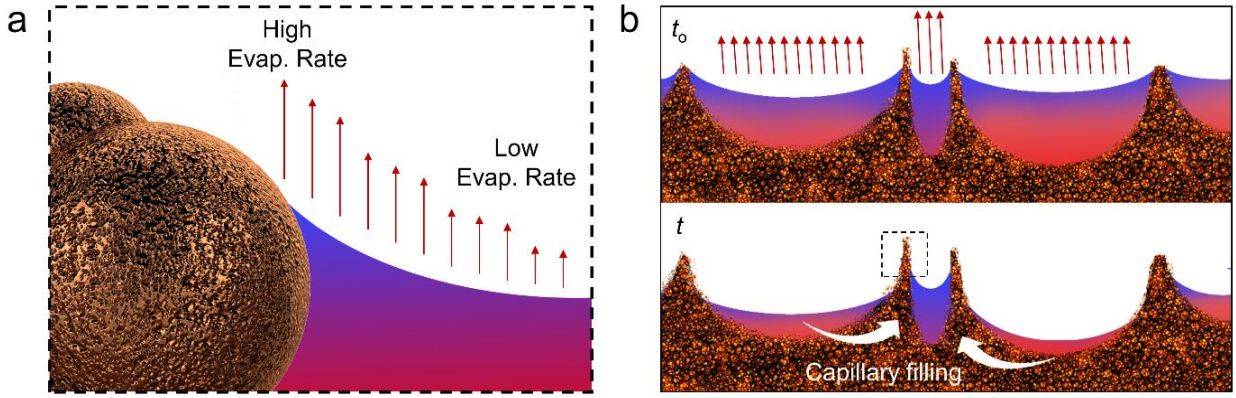

FIGURE 6: EVAPORATION-INDUCED LIQUID FLOW PATHS WITHIN MICROSCALE STRUCTURES. (a) The local evaporation rate near the liquid-vapor-solid contact line is higher than the local evaporation rate of the bulk liquid. (b) The illustrations show capillary filling into microcavities with smaller feature sizes where t_o is the initial state after liquid is wicked and t is an arbitrary state during the evaporation process.

4.4 Limitations of Estimating Liquid-Vapor Interface Effects

Obtaining accurate liquid-vapor interfaces between local sub-micron features is crucial in collecting accurate surface temperature profiles. The random, tortuous nature of the microstructures used in this study obscure sideview visualization and complicate experimental or computational meniscus shape regeneration. Therefore, we assume the influence of microscopic liquid thickness variations caused by the liquid-vapor interface between the microstructures are relatively small compared to that of bulk liquid thickness in Figure 2d. Nevertheless, obtaining an accurate liquid-vapor interface model will provide a better understanding of the geometrical features of the meniscus and therefore help define a more robust micro regime. With our definition, we acquire a relatively large temperature difference (~6°C) between the micro regime and the bulk liquid. To address these limitations, future work will include a more reliable analysis of the meniscus shape and its effect on fluorescence intensity by utilizing controlled microstructures such as micropillars.

5. CONCLUSION

In conclusion, we analyze the local and average evaporative performances of microstructures using μLIF techniques at the submicron scales. We show the potential of employing μLIF techniques for evaporation characterizations by separating the interplaying parameters such as temperature, liquid thickness, and dye concentration of rhodamine B solutions. A series of techniques involving dynamic surface-tracking and static focal plane measurements of fluorescence signals have been demonstrated to characterize overall and local liquid dry-outs. Furthermore, we show that submicron level evaporation rates can be measured by retrieving surface temperature information converted from fluorescence signals. The integrated results infer that liquid between nanoconfined features with small characteristic lengths exhibits higher evaporation rates with slow drying rates. The high evaporation rate associated with small characteristic lengths is caused by the influence of the micro regime located near (~0.3 – 1 μm) the solid-vapor-liquid contact lines. The slower drying rates might be attributed to the continuous liquid supply from the vicinity through capillary feeding. The μLIF techniques introduced in this work will enable researchers to precisely characterize microscale thermofluidic properties in thermal/fluid applications. Further work is needed to define the micro regime of the meniscus.

ACKNOWLEDGEMENTS

The work was sponsored by the National Science Foundation (NSF), (CBET-TTP 1752147, Dr. Jose Lage, the Program Director, Thermal Transport Processes). The authors acknowledge the valuable support from the Laboratory for Fluorescence Dynamics' (LFD), where the characterization was performed. Y.S. is thankful for the financial support from the UC Irvine Mechanical and Aerospace Engineering Department Graduate Fellowship.

REFERENCES

[1] Pop, E., 2010, "Energy Dissipation and Transport in Nanoscale Devices," *Nano Research*, Vol.(3) No.(3), pp. 147-169.

[2] Faghri, Amir %J Journal of heat transfer, 2012, "Review and advances in heat pipe science and technology," Vol.(134) No.(12), pp. 123001.

[3] Launay, S., Sartre, V., and Bonjour, J., 2007, "Parametric analysis of loop heat pipe operation: a literature review," *International Journal of Thermal Sciences*, Vol.(46) No.(7), pp. 621-636.

[4] Yeh, C. C., Chen, C. N., and Chen, Y. M., 2009, "Heat transfer analysis of a loop heat pipe with biporous wicks," *International Journal of Heat and Mass Transfer*, Vol.(52) No.(19-20), pp. 4426-4434.

[5] Weisenseel, Bastian, Greil, Peter, and Fey, Tobias %J Advanced Engineering Materials, 2017, "Biomorphous Silicon Carbide as Novel Loop Heat Pipe Wicks," Vol.(19) No.(1), pp. 1600379.

[6] Huminic, G., Huminic, A., Morjan, I., and Dumitrache, F., 2011, "Experimental study of the thermal performance of thermosyphon heat pipe using iron oxide nanoparticles," *International Journal of Heat and Mass Transfer*, Vol.(54) No.(1-3), pp. 656-661.
[7] Bodla, K. K., Weibel, J. A., and Garimella, S. V., 2013, "Advances in Fluid and Thermal Transport Property Analysis and Design of Sintered Porous Wick Microstructures," *Journal of Heat Transfer-Transactions of the Asme*, Vol.(135) No.(6).
[8] Kandlikar, S. G., 2017, "Enhanced Macroconvection Mechanism With Separate Liquid-Vapor Pathways to Improve Pool Boiling Performance," *Journal of Heat Transfer-Transactions of the Asme*, Vol.(139) No.(5).
[9] Li, T., and Peterson, G. P., 2006, "Evaporation/boiling in thin capillary wicks (II) - Effects of volumetric porosity and mesh size," *Journal of Heat Transfer-Transactions of the Asme*, Vol.(128) No.(12), pp. 1320-1328.
[10] Ranjan, Ram, Murthy, Jayathi Y, Garimella, Suresh V, Vadakkan, Unnikrishnan %J International Journal of Heat, and Transfer, Mass, 2011, "A numerical model for transport in flat heat pipes considering wick microstructure effects," Vol.(54) No.(1-3), pp. 153-168.
[11] Girard, F., Antoni, M., and Sefiane, K., 2010, "Infrared Thermography Investigation of an Evaporating Sessile Water Droplet on Heated Substrates," *Langmuir*, Vol.(26) No.(7), pp. 4576-4580.
[12] Hohmann, C., and Stephan, P., 2002, "Microscale temperature measurement at an evaporating liquid meniscus," *Experimental Thermal and Fluid Science*, Vol.(26) No.(2-4), pp. 157-162.
[13] Buffone, C., and Sefiane, K., 2005, "Temperature measurement near the triple line during phase change using thermochromic liquid crystal thermography," *Experiments in Fluids*, Vol.(39) No.(1), pp. 99-110.
[14] Pan, Z. H., Dash, S., Weibel, J. A., and Garimella, S. V., 2013, "Assessment of Water Droplet Evaporation Mechanisms on Hydrophobic and Superhydrophobic Substrates," *Langmuir*, Vol.(29) No.(51), pp. 15831-15841.
[15] Wang, H., Pan, Z. H., and Garimella, S. V., 2011, "Numerical investigation of heat and mass transfer from an evaporating meniscus in a heated open groove," *International Journal of Heat and Mass Transfer*, Vol.(54) No.(13-14), pp. 3015-3023.
[16] Mishan, Y., Mosyak, A., Pogrebnyak, E., and Hetsroni, G., 2007, "Effect of developing flow and thermal regime on momentum and heat transfer in micro-scale heat sink," *International Journal of Heat and Mass Transfer*, Vol.(50) No.(15-16), pp. 3100-3114.
[17] Carlomagno, G. M., and Cardone, G., 2010, "Infrared thermography for convective heat transfer measurements," *Experiments in Fluids*, Vol.(49) No.(6), pp. 1187-1218.
[18] Christofferson, J., Maize, K., Ezzahri, Y., Shabani, J., Wang, X., and Shakouri, A., 2007, "Microscale and nanoscale thermal characterization techniques," *2007 International Conference on Thermal Issues in Emergingtechnologies - Theory and Applications*, pp. 3-+.
[19] Dhavaleswarapu, H. K., Garimella, S. V., and Murthy, J. Y., 2009, "Microscale Temperature Measurements Near the Triple Line of an Evaporating Thin Liquid Film," *Journal of Heat Transfer-Transactions of the Asme*, Vol.(131) No.(6).
[20] Low, P., Kim, B., Takama, N., and Bergaud, C., 2008, "High-spatial-resolution surface-temperature mapping using fluorescent thermometry," *Small*, Vol.(4) No.(7), pp. 908-914.
[21] Kenning, D. B. R., and Yan, Y. Y., 1996, "Pool boiling heat transfer on a thin plate: Features revealed by liquid crystal thermography," *International Journal of Heat and Mass Transfer*, Vol.(39) No.(15), pp. 3117-&.
[22] Ekkad, S. V., and Han, J. C., 2000, "A transient liquid crystal thermography technique for gas turbine heat transfer measurements," *Measurement Science and Technology*, Vol.(11) No.(7), pp. 957-968.
[23] Brites, C. D. S., Lima, P. P., Silva, N. J. O., Millan, A., Amaral, V. S., Palacio, F., and Carlos, L. D., 2012, "Thermometry at the nanoscale," *Nanoscale*, Vol.(4) No.(16), pp. 4799-4829.
[24] Tovee, P. D., and Kolosov, O. V., 2013, "Mapping nanoscale thermal transfer in-liquid environment-immersion scanning thermal microscopy," *Nanotechnology*, Vol.(24) No.(46).
[25] Assy, A., and Gomes, S., 2015, "Temperature-dependent capillary forces at nano-contacts for estimating the heat conduction through a water meniscus," *Nanotechnology*, Vol.(26) No.(35).
[26] Wilson, A. A., and Sharar, D. J., 2018, "Temperature-Dependent Adhesion Mechanisms of Metal and Insulator Probe-Sample Contact Pairs," *Proceedings of the 17th Ieee Intersociety Conference on Thermal and Thermomechanical Phenomena in Electronic Systems (Itherm 2018)*, pp. 240-245.
[27] Martinek, J., Klapetek, P., and Campbell, A. C., 2015, "Methods for topography artifacts compensation in scanning thermal microscopy," *Ultramicroscopy*, Vol.(155) pp. 55-61.
[28] Menges, F., Mensch, P., Schmid, H., Riel, H., Stemmer, A., and Gotsmann, B., 2016, "Temperature mapping of operating nanoscale devices by scanning probe thermometry," *Nature Communications*, Vol.(7).
[29] Rochlitz, H., and Scholz, P., 2018, "Application of laser-induced fluorescence technique in a duct flow with one heated wall," *Experiments in Fluids*, Vol.(59) No.(3).
[30] Volkov, R. S., and Strizhak, P. A., 2017, "Planar laser-induced fluorescence diagnostics of water droplets heating and evaporation at high-temperature," *Applied Thermal Engineering*, Vol.(127) pp. 141-156.
[31] Chaze, W., Caballina, O., Castanet, G., and Lemoine, F., 2017, "Spatially and temporally resolved measurements of the temperature inside droplets impinging on a hot solid surface," *Experiments in Fluids*, Vol.(58) No.(8).
[32] Feng, J., Xiong, L., Wang, S. Q., Li, S. Y., Li, Y., and Yang, G. Q., 2013, "Fluorescent Temperature Sensing Using Triarylboron Compounds and Microcapsules for Detection of a Wide Temperature Range on the Micro- and Macroscale," *Advanced Functional Materials*, Vol.(23) No.(3), pp. 340-345.

[33] Erickson, D., Sinton, D., and Li, D. Q., 2003, "Joule heating and heat transfer in poly(dimethylsiloxane) microfluidic systems," *Lab on a Chip*, Vol.(3) No.(3), pp. 141-149.
[34] Samy, R., Glawdel, T., and Ren, C. L., 2008, "Method for microfluidic whole-chip temperature measurement using thin-film poly(dimethylsiloxane)/Rhodamine B," *Analytical Chemistry*, Vol.(80) No.(2), pp. 369-375.
[35] Glawdel, T., Almutairi, Z., Wang, S., and Ren, C., 2009, "Photobleaching absorbed Rhodamine B to improve temperature measurements in PDMS microchannels," *Lab on a Chip*, Vol.(9) No.(1), pp. 171-174.
[36] Ross, D., Gaitan, M., and Locascio, L. E., 2001, "Temperature measurement in microfluidic systems using a temperature-dependent fluorescent dye," *Analytical Chemistry*, Vol.(73) No.(17), pp. 4117-4123.
[37] Vetrone, F., Naccache, R., Zamarron, A., de la Fuente, A. J., Sanz-Rodriguez, F., Maestro, L. M., Rodriguez, E. M., Jaque, D., Sole, J. G., and Capobianco, J. A., 2010, "Temperature Sensing Using Fluorescent Nanothermometers," *Acs Nano*, Vol.(4) No.(6), pp. 3254-3258.
[38] Feng, J., Tian, K. J., Hu, D. H., Wang, S. Q., Li, S. Y., Zeng, Y., Li, Y., and Yang, G. Q., 2011, "A Triarylboron-Based Fluorescent Thermometer: Sensitive Over a Wide Temperature Range," *Angewandte Chemie-International Edition*, Vol.(50) No.(35), pp. 8072-8076.
[39] Sakakibara, J., Hishida, K., and Maeda, M., 1993, "Measurements of Thermally Stratified Pipe-Flow Using Image-Processing Techniques," *Experiments in Fluids*, Vol.(16) No.(2), pp. 82-96.
[40] Fikry, M., Omar, M. M., and Ismail, L. Z., 2011, "Effect of Host Medium on the Fluorescence Emission Intensity of Rhodamine B in Liquid and Solid Phase," *Modern Trends in Physics Research: Third International Conference on Modern Trends in Physics Research*, pp. 210-219.
[41] Greszik, D., Yang, H., Dreier, T., and Schulz, C., 2011, "Measurement of water film thickness by laser-induced fluorescence and Raman imaging," *Applied Physics B-Lasers and Optics*, Vol.(102) No.(1), pp. 123-132.
[42] Wang, H., Garimella, S. V., and Murthy, J. Y., 2007, "Characteristics of an evaporating thin film in a microchannel," *International Journal of Heat and Mass Transfer*, Vol.(50) No.(19-20), pp. 3933-3942.
[43] Bodla, K. K., Murthy, J. Y., and Garimella, S. V., 2013, "Evaporation analysis in sintered wick microstructures," *International Journal of Heat and Mass Transfer*, Vol.(61) pp. 729-741.
[44] Montazeri, K., Lee, H., and Won, Y., 2018, "Microscopic analysis of thin-film evaporation on spherical pore surfaces," *International Journal of Heat and Mass Transfer*, Vol.(122) pp. 59-68.